Published in final edited form as:

ACS Nano. 2019 September 24; 13(9): 9918–9926. doi:10.1021/acsnano.9b04231.

Chameleon-Inspired Strain-Accommodating Smart Skin

Yixiao Dong[†], **Alisina Bazrafshan**[†], **Anastassia Pokutta**[‡], **Fatiesa Sulejmani**[‡], **Wei Sun**[‡], **J. Dale Combs**[†], **Kimberly C. Clarke**[†], **Khalid Salaita**[*,†]

[†]Department of Chemistry, Emory University, Atlanta, GA, USA.

[‡]Wallace H. Coulter Department of Biomedical Engineering, Georgia Institute of Technology, GA, USA.

Abstract

Stimuli-responsive color-changing hydrogels, commonly colored using embedded photonic crystals (PCs), have potential applications ranging from chemical sensing to camouflage and anti-counterfeiting. A major limitation in these PC hydrogels is that they require significant deformation (>20%) in order to change the PC lattice constant and generate an observable chromatic shift (~100 nm). By analyzing the mechanism of how chameleon skin changes color, we developed a strain-accommodating smart skin (SASS), which maintains near-constant size during chromatic shifting. SASS is comprised of two types of hydrogels: a stimuli-responsive, PC-containing hydrogel that is patterned within a second hydrogel with robust mechanical properties, which permits strain-accommodation. In contrast to conventional "accordion"-type PC responsive hydrogels, SASS maintains near constant volume during chromatic shifting. Importantly, SASS materials are stretchable (strain ~ 150%), amenable to patterning, spectrally tunable, and responsive to both heat and natural sunlight. We demonstrate examples of using SASS for biomimicry. Our strategy, to embed responsive materials within a mechanically-matched scaffolding polymer, provides a general framework to guide the future design of artificial smart skins.

Keywords

magnetic particles; chameleon inspired structural color; light responsive hydrogels; strain accommodating; photonic crystals; chromatic materials

---

[*]**Corresponding Author** k.salaita@emory.edu.

Author Contributions

Y. D. and K. S. conceived of the project. Y. D. designed and performed most of the experiments. A.A. helped with the design of Delrin mold and gel cutting tools. A. P., F. S., and W. S. helped with the uniaxial tensile measurements. J. C. and K. C. participated in discussion and revision of the paper. Y. D. and K. S. wrote the manuscript.

Supporting Information.

The following files are available free of charge. on the ACS Publications website at DOI: 10.1021/acsnano.9b04231.

Detailed materials and methods; Finite element analysis; Characterization of Fe_3O_4@SiO_2 nanoparticles; Optical microscope imaging; Calculation of photo-thermal efficiency of MNPs; Comparison of size change of fish-shaped conventional RPC to fish-shaped SASS (PDF)

Financial interest.

The authors declare no competing interest.

Many living creatures have evolved the ability to change color, such as chameleons[1], neon tetra fishes,[2,3] and Morpho Sulkowskyi butterflies.[4,5] The ability to rapidly change color is beneficial for camouflage, mating, and intimidating predators. Coloration in these organisms is described as “structural” because it is generated by periodic arrays of nano- and micro-structures, known as photonic crystals (PCs), which generate color through optical interference effects. Unlike common coloration strategies using dyes and pigments, which rely on wavelength-specific absorption of light, structural coloration is immune to photobleaching and can be easily manipulated by controlling particle spacing as opposed to synthetic strategies. In accordance with Bragg’s law of diffraction,[6,7] the periodic distance between elements in these natural PCs dictates the color of the material. Accordingly, the mechanism of dynamic color change for many of these species employs responsive matrices that tune the spacing of the PCs.

Inspired by natural examples, there has been significant effort focused on generating synthetic responsive PC materials that can change color on demand.[8-13] Such color-changing materials, which are sometimes described as “smart skins”, are envisioned to become important in various applications ranging from camouflage and communications to anti-counterfeiting and biosensing. The fundamental mechanism for adjusting the color of synthetic PCs mirrors that of natural systems and requires modulating the periodicity of the PC lattice using an “accordion” mechanism.[14-17] This strategy is usually realized by embedding the PC in a hydrogel[18-21] or flexible polymer matrix[22,23] that responds to an input by expansion or contraction, resulting in a shift in the PC periodicity. The major problem with this accordion strategy of creating artificial smart skins pertains to the large volume change, which leads to structural instability and buckling of the material.[24,25] For example, a 20% or greater linear expansion or contraction (strain) of a responsive PC is required to produce a significant color shift ($\Delta\lambda$ =100 nm) (Supplementary S1). This magnitude of strain and deformation impedes their application and adoption. However, this led us to consider how color-changing animals, such as chameleons address this problem (Figure 1a). Based on recent time-lapse imaging of chameleon skin,[1] we noticed that only a small fraction of the skin cells contain the guanine PC arrays, while the remainder of the skin cells are colorless. In other words, chameleon skin tissue included non-responsive cells that may contribute to reduce the global volume change during chromatic response.

This general concept is shown in Figure 1b, which highlights the contrast between artificial responsive PCs that have been extensively studied, and natural responsive PCs, which employ a tunable PC element embedded within a matrix that lacks PCs and accommodates the strain. This structural difference, which was shown in natural responsive PCs, leads to a significant reduction in the total change in volume of the material, while maintaining the observable dynamic coloration.

Herein, we demonstrate a strain-accommodating smart skin (SASS) inspired by the structure of natural responsive PCs. The total volume of our SASS structure is maintained because the PC contraction is accommodated by local elastic deformation of a supporting polymer layer. SASS materials display excellent mechanical properties including high stretchability and good mechanical strength that is dependent, primarily, on the supporting layer. SASS demonstrates a generalizable concept of how to create responsive PCs that maintain constant size during chromatic shifting. Furthermore, we show that SASS color-change can be optically triggered and SASS films rapidly changed color upon exposure to ambient sunlight ($t = 10$ min). These features suggest the potential utility of SASS in applications such as camouflage and anti-counterfeiting.

RESULTS AND DISCUSSION

To recapitulate the strain-accommodating behavior of natural responsive PCs and predict the optimal material design, we first performed finite element analysis modeling of mechanical strain. Specifically, we modeled a patterned array of responsive PC hydrogels that were embedded within a non-responsive supporting polymer layer (Figure 1c and 1d, also see Figure S1 in supplementary S2). The geometry of the model was such that the responsive PC elements were localized to the top face of the material. When we fixed the Young's modulus of the two materials and assumed a 50% change in length of the responsive layer, we found that a single planar layer of responsive hydrogel placed atop a supporting layer led to significant strain and deformation at the edges (Figure 1d, 1×1 case). Note that in our model, a free-standing responsive hydrogel film displayed the expected deformation (Figure S2). Importantly, when we segmented the responsive layer into arrays of squares, our modeling predicted a significant dampening of the deformation/strain that is associated with increasing number of segments (Figure 1d, 1×1, 5×5, 9×9, 13×13, and 17×17 cases). This reduction in deformation diminishes as n was increased from 13×13 to 17×17 as the SASS material showed minimal deformation with n=17. Plots of the Von-mises forces applied on a chosen plane of the supporting layer as a function of the number of square arrays predict a monotonic relationship, where the more finely patterned responsive polymer structure displayed the lowest displacement and average force (Figure S3, S4 and Figure 1e). Note that this conclusion holds as we vary the Young's modulus of the responsive and supporting layers and is not specific to the values shown in these representative modeling results. Therefore, our models predict that embedding finely segmented responsive PC layer within an elastic supporting layer will greatly diminish the global strain.

Guided by the computational results, we fabricated SASS as shown in Figure 1f. The responsive PC layer was comprised of monodisperse $Fe_3O_4@SiO_2$ particles (180 nm diameter, Figure S5 and S6), fabricated as previously described,[26] organized periodically using an external magnetic field, and confined within a photo-crosslinked poly(*N*-isopropylacrylamide) (pNIPAM) polymer. For optimal design of SASS, it is important to select a supporting polymer that is non-responsive while displaying robust mechanical elasticity. As a proof-of-concept, we employed tetra-polyethylene glycol (PEG) doped with a nanoclay (Laponite XLG) to create a robust hydrogel[27] as the supporting layer.

SASS fabrication is detailed in Figure 1g. Briefly, $Fe_3O_4@SiO_2$ nanoparticles were mixed with the pNIPAM precursor solution (PEGDA crosslinker, riboflavin photoinitiator, NIPAM monomer), and while applying a magnetic field, UV light was used to crosslink the hydrogel, thus locking nanoparticles into defined periodic arrays. Subsequently, a mold (Figure S7) was used to create a square array of responsive PC hydrogels (4×4 mm squares, spaced by 0.5 mm). Finally, the tetra-PEG supporting layer precursor was cured onto the responsive PC array at room temperature. A photograph of a SASS film with a 5×5 responsive PC array demonstrating its color and elasticity is shown in Figure 1f. Cross-section scanning electron microscopy (SEM) imaging of the responsive PC layer confirms a periodic chain structure formed by magnetic nanoparticles (MNPs) (Figure 1g), which generates the colorful Bragg diffraction of the sample. Notably, the chain structures appear to be distorted in the SEM images likely due to drying-induced compression of the hydrogel matrix during imaging.

To optimize the chromatic shift of the responsive pNIPAM PC layer, we tested the role of its mechanical properties (crosslinker concentration) in tuning the swelling/deswelling ratio (Figure 2a) and generating a maximal chromatic shift (Figure 2b). Optimization was performed using a reflection-mode spectrometer to record the chromatic shift of pNIPAM PC films in response to thermal heating (45 °C). We found that an intermediate concentration of crosslinker (120 mM polyethylene glycol diacrylate, PEGDA) produced the greatest magnitude of chromatic shift while minimizing area change. Additionally, optimization of magnetic field strength during synthesis is shown in Figure 2c. We found that if the magnetic field was too strong (385 Gauss), the peak wavelength shift was diminished likely because the periodic distance between particles approaches a minimum, and the collapse of the responsive hydrogel no longer can reduce inter-particle distance further. On the contrary, if the magnetic field is too weak (175 Gauss), no color is observed since the field strength is not sufficient to assemble photonic crystal. (Figure 2c). Therefore, we fixed our protocol to use 245 Gauss as it produced a maximum chromatic shift.

These experiments provided the optimal parameters for fabricating the responsive PC hydrogel. Using these optimized conditions, we measured the thermally-induced volume transition of PC-containing and non-PC containing responsive films as shown in Figure 2d (120 mM PEGDA, 245 Gauss). PC-containing gels displayed a sharper and more significant thermally-induced deswelling strain compared to the pNIPAM films lacking the MNPs. This may be due to the strong UV absorption cross-section of MNPs which impacts UV-initiated radical polymerization. Note that the volumetric transition of these films is broader compared to that of conventional pNIPAM films, which is likely due to the PEG chains in the crosslinker (PEGDA) that modulates dehydration of the hydrogel (Figure 2d). The data in Figure 2a supports this conclusion since gels with higher PEGDA concentrations display lower deswelling ratios.

Representative reflection spectra and plots of the peak reflection wavelength *versus* temperature of the as-prepared SASS samples show a clear thermo-chromatic shift, in agreement with the reported behavior of responsive hydrogels (Figure 2e and f).[28,29] The heat-triggered response of the SASS film was similar to that of the responsive PC films suggesting that the SASS architecture did not significantly modulate the transition temperature of pNIPAM. However, compared to the mechanical strength of conventional pNIPAM hydrogels,[30] which display rupture forces of a few kPa, SASS displayed superior mechanical strength. Specifically, uniaxial tensile testing (Figure 2g) showed that SASS has a rupture force of 60 kPa with a strain of 1.5. This was primarily driven by the mechanical properties of the supporting layer, which similarly had a 83 kPa rupture force with strain of 1.8. We also found that SASS samples could be handled manually and displayed a color change upon stretching (Figure 2h). Note that the chromatic shift generated by the

Fe_3O_4@SiO_2 particle chains are sensitive to the orientation of the mechanical strain. Given that the thermal or optically triggered deswelling response generates in-plane forces, we focused on strains parallel to the SASS film. Of course, one can apply an external strain that is perpendicular to the SASS film, and such forces can lead to an opposite red-shift in the reflection peak of the material.

Critically, SASS displayed significant strain-accommodating behavior as was especially clear when comparing its volume transition to conventional responsive PC films (Figure 2i). To illustrate the difference, SASS and conventional responsive PC films were sandwiched between two plastic petri dishes such that only in-plane deformations were allowed. To the best of our ability to measure the dimensions of the SASS sample, its size was identical following heating-induced chromatic shifting, while the length of the conventional responsive PC film was reduced by ~23% after responding to the same heating source. Supplementary Figure S9 shows the deformation of free-standing SASS films with 1×1 and 8×8 segmentation (supplementary S3). The 1×1 SASS film undergoes curling to form a tube-like structure due to the strain, in contrast to the 8×8 film that displays significant reduced strain.

In addition to its thermoresponsive properties, another intriguing feature of SASS is its light responsive behavior. Due to the strong light absorption of magnetite nanoparticles (Figure S7),[31] we hypothesized that illumination of SASS would also trigger a chromatic response (Figure 3a). Upon exposure of SASS to a handheld white light LED source, we observed a rapid and reversible reflectance peak shift that mirrored the response to thermal heating (Figure 3b and c). In the samples tested, we found that the reflection λ_{max} of SASS shifted from 600 nm to 525 nm within a few minutes of illumination. To further quantify the photo-thermal conversion efficiency of MNPs, a calibrated 370 nm light source with ~20mW/cm^2 intensity was used to heat an aqueous dispersion of MNPs in a quartz cuvette (schematic shown in Figure 3d). As plotted in Figure 3e, the photo-thermal ideal heating rate can be inferred by extrapolating a tangential line to the initial phase of the heating curve. Combining this data with the equations shown in the supporting information (Supplementary S4), we inferred a conversion efficiency of 81.8%.

We next aimed to validate the dynamic re-modeling of the PC arrays within the responsive hydrogel film upon illumination. To achieve this, we employed high-resolution *in-situ* optical microscopy to excite and simultaneously image the PC layer within the SASS film (Figure 4a). We found that exciting the sample using a 405 nm laser coupled with a quad cube filter set (405/488/561/647) revealed the weak autofluorescence of the hydrogel. By happenstance, we found that continuous illumination in the 405 nm channel also triggered photo-thermal heating, localized deswelling of the SASS film, and reorganization of the PC microstructure (Figure 4b). Conveniently, the nanochain structure has significant scattering when imaged using a 535 nm reflection interference contrast microscopy (RICM) filter set. This allowed for concurrent imaging of the PC nanostructures along with the surrounding responsive hydrogel during photothermal heating and cooling (Figure 4c). As expected, the PC arrays (RICM channel) were anti-localized with the polymer hydrogel (405 nm channel). End points and Time lapse images recording a single photothermal heating/cooling cycle are shown in Figure 4b and 4c (also see Supplementary Movie S1 and S2). In the time lapse images, the heating phase (0-13.9 s) was recorded using the 405 nm channel, while the cooling phase (13.9-27.8 s) was captured in the RICM channel. The PC chains are displaced and indeed go out of focus due to the isotropic (3D) nature of deswelling. Importantly, the images comparing the positions of the nanochain structure before and after the heating/ cooling cycle demonstrate that the SASS microstructure recovers to its initial configuration.

To confirm that the photo-thermal effect was exclusively attributed to absorption by $Fe_3O_4@SiO_2$ particles rather than other components of SASS, we fabricated SASS films doped with pure silica particles lacking the Fe_3O_4 core (Figure 4d), and compared the time-dependent PC array displacement in SASS samples to that of films with silica nanoparticles (Figure 4e and Figure S11, also see Supplementary Movie S3 and S4). The lack of response in the silica nanoparticle-containing samples confirms the key role of magnetite in driving the light-triggered chromatic response of SASS.

SASS chromatic response could also be spatially controlled using localized illumination. To demonstrate this capability, a 532 nm laser was focused onto a 2 mm diameter spot on the SASS sample at an angle of 50° and a smart phone camera was used to record the chromatic change perpendicular to the sample (Figure 5a). The sample drastically changed color within a few seconds of laser illumination (Figure 5a, also see Supplementary Movie S5), and the color change was localized to the spot of irradiation. The response was quantified by RGB analysis of the images (Figure 5b). An increase in blue intensity was observed with a concomitant decrease in both red and green intensity. This response is consistent with the expected blue shift in the reflection spectra after deswelling. This result suggests potential applications for SASS involving dynamic chromatic patterning.

Neon tetra fish are well known for their light-responsive behavior where the lateral stripes display different structural colors after brief exposure to sunlight (Figure 5c).[2,3] To mimic this response, we first tested whether SASS is sensitive to natural sunlight. Surprisingly, we found that a 10 min exposure to sunlight triggered an observable chromatic shift (Figure 5d). Specifically, the SASS reflection λ_{max} shifted from 622±2.2 nm to 573±7.7 nm for samples fabricated with 210 nm diameter MNPs. The response triggered by sunlight was reversible, as the amplitude of the chromatic shift (48±9.6 nm) did not change significantly over the course of six illumination/cooling cycles. The range of the λ_{max} shift response could also be tuned by employing MNPs of a different diameter. For example, particles with a 180 nm diameter showed a reflection λ_{max} of 556±10.1 nm that reversibly shifts to 504±5.3 nm upon sunlight exposure (Figure 5e). Further mimicking the neon tetra fish response, we fabricated SASS films shaped like a fish (Figure 5f). After a 10 min exposure to natural sunlight, the SASS film shifted from orange to green, while the overall size remained constant as determined to the best of our abilities (Figure S12).

Given that SASS can be fabricated in different shapes and is sunlight responsive, we aimed to demonstrate camouflage behavior. Hence, we fabricated a leaf-shaped SASS sample and arranged it together alongside real leaves (Figure 5g). After exposure to sunlight, the color of the SASS “leaf” shifted from orange to green and was camouflaged among the real leaves. Again, a key feature enabling camouflage is that the size of the “leaf” remained constant during chromatic shifting.

CONCLUSIONS

In summary, we present an alternative approach to fabricate smart skin materials inspired by the chameleon skin structure. The SASS design solves the long-standing problem of mechanical buckling and instability of conventional responsive PC hydrogels. The key element to SASS is a two-component polymer material, where a segmented responsive PC hydrogel is embedded within a supporting polymer that accommodates the strain arising from the volume transition. By optimizing crosslinker concentration and magnetic field strength, we demonstrate a strong and reversible heat/light triggered optical response in SASS. High resolution optical microscopy confirms light-triggered local deswelling and chromatic response of the SASS film. Moreover, SASS chromatic response can be controlled in space and time using a focused laser beam. Note that the resolution of patterning is limited by the dimensions of the illumination spot, the rate of gel response, and the thermal diffusion coefficient within the sample. Future work will define these parameters. Finally, we show that SASS is sensitive to natural sunlight and can be molded into various geometries to aid in biomimicry. This suggests potential applications in camouflage, signaling, and anti-counterfeiting.

METHODS

Synthesis of Fe_3O_4@SiO_2 core-shell nanoparticles (MNPs).

Fe_3O_4@SiO_2 core-shell nanoparticles were synthesized according to previously developed methods.[26] Briefly, for particles with an average diameter of 180 nm, 0.65 g $FeCl_3$, 40 mL ethylene glycol, 3.0 g sodium acetate, 1.05 g Poly(4-styrenesulfonic acid-co-maleic acid) sodium salt, 14 mg D-isoascorbic acid, and 120 μL deionized H_2O were added consecutively into a parafilm sealed beaker. After vigorous magnetic stirring for about 40 min, a homogeneous mixture formed and then 0.6 g NaOH was added. The mixture was stirred for 1-2 h until all the NaOH was completely dissolved. The mixture was then transferred into a capped 50 mL Erlenmeyer flask and then allowed to react in a preheated oven (190 ˚C) for 9 h. The particles were washed with 30 mL of 50% ethanol three times, and then washed three additional times with DI water.

To synthesize the silica shell, a 12 mL aliquot of Fe_3O_4 dispersion was mixed with 80 mL ethanol and 4 mL ammonium hydroxide (25-28 wt%) under vigorous mechanical stirring for 1 min. This solution was warmed by using a water bath at 50 ˚C. Subsequently, two aliquots of 0.4 mL TEOS were added every 20 min. Finally, the reaction products were washed with ethanol three times by using magnetic separation for each wash.

Synthesis of pure silica nanoparticles.

Silica nanoparticles (~300 nm) were synthesized by the well-established stöber method.[32] 50 mL ammonium solution was made by mixing 9 mL ammonium hydroxide (25-28 wt%), 16 mL ethanol, and 25 mL deionized H_2O. This solution was swiftly added to 50 mL of 0.4 M TEOS ethanol solution under vigorous stirring. After reacting for 2h, the particles were centrifuged and washed three times with ethanol to collect monodisperse silica nanoparticles. TEM indicated that the average particle size was approximately 300 nm.

Fabrication of Delrin® mold and gel cutting tools.

Square shaped sheets of Delrin® with a thickness of 0.125 inches (0.3175 cm) were cut into the desired shapes using a laser cutter (Universal Laser Systems VLS 4.60, featuring a 60-watt CO_2 laser). The patterns were designed using the AutoCAD software package.

Synthesis of responsive photonic film.

The as-obtained $Fe_3O_4@SiO_2$ particles from the protocol (described above) were redispersed in 12 mL of ethanol, and then 3 mL of this solution of $Fe_3O_4@SiO_2$ was redispersed in EG solution containing 8 mg riboflavin, followed by adding 0.09 g Irgacure, 225 μL poly(ethylene glycol) diacrylate, and 0.45 g N-isopropylacrylamide. The mixture was vortexed for 10 s to obtain a homogeneous solution that was then sonicated for 5 min in the dark. We describe this mixture as the "precursor solution" in subsequent steps. A 3 cm × 3 cm Delrin mold covered with a piece of transparent petri dish was used to fabricate the responsive photonic crystal layer. For each synthesis, 350 μL precursor solution was injected into the mold and exposed to a magnetic field of approximately 245 Gauss (determined using a WT10A teslameter). Finally, the precursor solution was cured with a 100 W high intensity UV lamp (365 nm, Analytik Jena US company) for 10 min. The as-obtained thin film was washed with DMF and H_2O three times, respectively, then was stored in water for further use. Notably, for special shapes (fish and leaf), the Delrin® molds were deliberately fabricated into the required shapes by using a laser cutter as described above using AutoCAD to draw the design.

Patterning of SASS.

The as-synthesized responsive photonic film was first cut by firmly pressing a patterned Delrin® grid. This was performed on a clean petri dish surface. Prior to the fabrication of the PEG supporting layer, two precursor solutions were prepared. The first (precursor A) was generated using 750 μL deionized water and 0.03 g Laponite XLG that were mixed together in a 2 mL vial using a magnetic stir bar until the solution became clear. To this Laponite XLG solution, 750 μL of 0.1 M $Na_4P_2O_7/H_3PO_4$ buffer (pH=7.2) and 0.12 g tetra-PEG-NH_2 were added and completely dissolved through vigorous stirring and sonication. The second precursor solution (B) was prepared using 0.12 g tetra-PEG-NHS that was dissolved in 600 μL $Na_4P_2O_7/H_3PO_4$ buffer (pH=7.2) under vigorous stirring and sonication. Both precursors A and B were stored in an ice box for 20 min before mixing in order to slow the gelation rate. After cooling precursors A and B, the solutions were mixed together for 10 s using a magnetic stir bar, then quickly poured into a specific Delrin® mold (Figure S4) and sandwiched with the grid-cut photonic film that was placed on a petri dish. The gelation process was complete within 15 min at room temperature. More details of materials and fabrication process are shown in Supporting information.

Characterization.

TEM images were acquired with an Hitachi HT-7700 with 80 kV accelerating voltage. SEM images were obtained using a Topcon DS-130F Field Emission SEM. Digital photographs and videos were recorded with an iPhone 6s. Dynamic surface temperature was monitored by an Etekcity Lasergrip 1080 Non-Contact Digital Laser Infrared Thermometer

Temperature Gun (dynamic range for instrument is −50 ˚C to 550 ˚C). Dynamic light scattering (DLS) was performed with a NanoPlus Zeta / Nano Particle Analyzer at 25 °C. UV light intensity was determined by AMTAST UVA365 UV light meter. Gel deswelling ratio was measured by a digital caliper. White LED illumination was performed using a Cygolite Metro 800 with light intensity of 800 lumen (distance to the sample: 3 cm). Solar responses were tested with natural sunlight during the daytime between the hours of 1 pm to 3 pm during the months of June and July (location: 33°47'29.6"N 84°19'36.3"W). Laser response test was conducted with a 50-80 mW 532 nm Green Laser Module with TTL and Fan (12V) purchased from OdicForce Lasers (Surbiton, UK). Reflectivity spectra were measured with a FLAME-S-VIS-NIR Spectrometer equipped with a premium 400 μm reflection probe (Ocean optics Inc., Dunedin, FL). All the spectra data were recorded through the OceanView 1.6.3 software package. Uniaxial tensile tests were conducted using a TestResources 100Q Universal Testing Machine (Shakopee, MN). All optical imaging was performed using a Nikon Eclipse *Ti* microscope, operated with Nikon Elements software, a 1.49 NA CFI Apo 100x objective, perfect focus system, LED light source along with a laser launch excitation source. ImageJ was used to analyze the intensity change of the time lapse video. Further experimental details are included in Supporting Information.

Supplementary Material

Refer to Web version on PubMed Central for supplementary material.

ACKNOWLEDGMENT

K.S. is grateful for support from the DARPA BTO (grant no. HR0011-16-2-0011), NIH R01 GM 131099, and NIH R01 GM 124472. This project was supported in part by the Robert P. Apkarian Integrated Electron Microscopy Core. We thank Dr. Huangzhang Zhang in Wuhan University of Technology for the critical help on modeling.

REFERENCES

1. Teyssier J; Saenko SV; van der Marel D; Milinkovitch MC, Photonic Crystals Cause Active Colour Change in Chameleons. Nat. Commun 2015, 6, 6368. [PubMed: 25757068]
2. Gur D; Palmer BA; Leshem B; Oron D; Fratzl P; Weiner S; Addadi L, The Mechanism of Color Change in the Neon Tetra Fish: a Light-Induced Tunable Photonic Crystal Array. Angew. Chem. Int. Ed 2015, 54, 12426–12430.
3. Yoshioka S; Matsuhana B; Tanaka S; Inouye Y; Oshima N; Kinoshita S, Mechanism of Variable Structural Colour in the Neon Tetra: Quantitative Evaluation of the Venetian Blind Model. J. Royal Soc. Interface 2010, 8, 56–66.
4. Niu S; Li B; Mu Z; Yang M; Zhang J; Han Z; Ren L, Excellent Structure-Based Multifunction of Morpho Butterfly Wings: A Review. J. Bionic. Eng 2015, 12, 170–189.
5. Tao L; Wenhong P; Shenmin Z; Di Z, Bio-Inspired Fabrication of Stimuli-Responsive Photonic Crystals with Hierarchical Structures and Their Applications. Nanotechnology 2016, 27, 122001. [PubMed: 26891477]
6. Aguirre CI; Reguera E; Stein A, Tunable Colors in Opals and Inverse Opal Photonic Crystals. Adv. Funct. Mater 2010, 20, 2565–2578.
7. Wu S, Xia H, Xu J, Sun X, Liu X, Manipulating Luminescence of Light Emitters by Photonic Crystals. Adv. Mater 2018, 30, 1803362.
8. Ge D; Lee E; Yang L; Cho Y; Li M; Gianola DS; Yang S, A Robust Smart Window: Reversibly Switching from High Transparency to Angle-Independent Structural Color Display. Adv. Mater 2015, 27, 2489–2495. [PubMed: 25732127]

9. Inan H; Poyraz M; Inci F; Lifson MA; Baday M; Cunningham BT; Demirci U, Photonic Crystals: Emerging Biosensors and Their Promise for Point-of-Care Applications. Chem. Soc. Rev 2017, 46, 366–388. [PubMed: 27841420]
10. Lee GH; Choi TM; Kim B; Han SH; Lee JM; Kim S-H, Chameleon-Inspired Mechanochromic Photonic Films Composed of Non-Close-Packed Colloidal Arrays. ACS Nano 2017, 11, 11350–11357. [PubMed: 29095594]
11. Zhang R; Wang Q; Zheng X, Flexible Mechanochromic Photonic Crystals: Routes to Visual Sensors and Their Mechanical Properties. J. Mater. Chem. C 2018, 6, 3182–3199.
12. Cai Z; Kwak DH; Punihaole D; Hong Z; Velankar SS; Liu X; Asher SA, A Photonic Crystal Protein Hydrogel Sensor for Candida Albicans. Angew. Chem. Int. Ed 2015, 54, 13036–13040.
13. Cai Z; Zhang J-T; Xue F; Hong Z; Punihaole D; Asher SA, 2D Photonic Crystal Protein Hydrogel Coulometer for Sensing Serum Albumin Ligand Binding. Anal. Chem 2014, 86, 4840–4847. [PubMed: 24766373]
14. Gur D; Leshem B; Farstey V; Oron D; Addadi L; Weiner S, Light-Induced Color Change in the Sapphirinid Copepods: Tunable Photonic Crystals. Adv. Funct. Mater 2016, 26, 1393–1399.
15. Cai Z; Luck LA; Punihaole D; Madura JD; Asher SA, Photonic Crystal Protein Hydrogel Sensor Materials Enabled by Conformationally Induced Volume Phase Transition. Chem. Sci 2016, 7, 4557–4562. [PubMed: 30155102]
16. Luo Z; Evans BA; Chang C-H, Magnetically Actuated Dynamic Iridescence Inspired by the Neon Tetra. ACS Nano 2019.
17. Isapour G; Lattuada M, Bioinspired Stimuli-Responsive Color-Changing Systems. Adv. Mater 2018, 30, 1707069.
18. Couturier JP; Sütterlin M; Laschewsky A; Hettrich C; Wischerhoff E, Responsive Inverse Opal Hydrogels for the Sensing of Macromolecules. Angew. Chem. Int. Ed 2015, 54, 6641–6644.
19. Luo W; Cui Q; Fang K; Chen K; Ma H; Guan J, Responsive Hydrogel-Based Photonic Nanochains for Microenvironment Sensing and Imaging in Real Time and High Resolution. Nano Lett. 2018 DOI: 10.1021/acs.nanolett.7b04218.
20. Ma H; Zhu M; Luo W; Li W; Fang K; Mou F; Guan J, Free-standing, Flexible Thermochromic Films Based on One-Dimensional Magnetic Photonic Crystals. J. Mater. Chem. C 2015, 3, 2848–2855.
21. Zhang J-T; Smith N; Asher SA, Two-Dimensional Photonic Crystal Surfactant Detection. Anal. Chem 2012, 84, 6416–6420. [PubMed: 22720790]
22. Schauer S; Baumberg JJ; Hölscher H; Smoukov SK, Tuning of Structural Colors Like a Chameleon Enabled by Shape-Memory Polymers. Macromol. Rapid Commun 2018, 39, 1800518.
23. Vatankhah-Varnosfaderani M; Keith AN; Cong Y; Liang H; Rosenthal M; Sztucki M; Clair C; Magonov S; Ivanov DA; Dobrynin AV, Chameleon-Like Elastomers with Molecularly Encoded Strain-Adaptive Stiffening and Coloration. Science 2018, 359, 1509–1513. [PubMed: 29599240]
24. Ye B-F; Zhao Y-J; Cheng Y; Li T-T; Xie Z-Y; Zhao X-W; Gu Z-Z, Colorimetric Photonic Hydrogel Aptasensor for the Screening of Heavy Metal Ions. Nanoscale 2012, 4, 5998–6003. [PubMed: 22936101]
25. Park J-G; Rogers WB; Magkiriadou S; Kodger T; Kim S-H; Kim Y-S; Manoharan VN, Photonic-Crystal Hydrogels with a Rapidly Tunable Stop Band and High Reflectivity Across the Visible. Opt. Mat. Express 2017, 7, 253–263.
26. Dong Y; Wen B; Chen Y; Cao P; Zhang C, Autoclave-Free Facile Approach to the Synthesis of Highly Tunable Nanocrystal Clusters for Magnetic Responsive Photonic Crystals. RSC Adv. 2016, 6, 64434–64440.
27. Fukasawa M; Sakai T; Chung U.-i.; Haraguchi K, Synthesis and Mechanical Properties of a Nanocomposite Gel Consisting of a Tetra-PEG/Clay Network. Macromolecules 2010, 43, 4370–4378.
28. Kang Y; Walish JJ; Gorishnyy T; Thomas EL, Broad-Wavelength-Range Chemically Tunable Block-Copolymer Photonic Gels. Nat. Mater 2007, 6, 957. [PubMed: 17952084]
29. Matsubara K; Watanabe M; Takeoka Y, A Thermally Adjustable Multicolor Photochromic Hydrogel. Angew. Chem. Int. Ed 2007, 46, 1688–1692.

30. Haq MA; Su Y; Wang D, Mechanical Properties of PNIPAM Based Hydrogels: A Review. Mater. Sci. Eng. C 2017, 70, 842–855.

31. Chen R; Zhu K; Gan Q; Yu Y; Zhang T; Liu X; Ye M; Yin Y, Interfacial Solar Heating by Self-Assembled Fe3O4@C Film for Steam Generation. Mater. Chem. Frontiers 2017, 1, 2620–2626.

32. Stöber W; Fink A; Bohn E, Controlled Growth of Monodisperse Silica Spheres in the Micron Size Range. J. Colloid Interface Sci 1968, 26, 62–69.

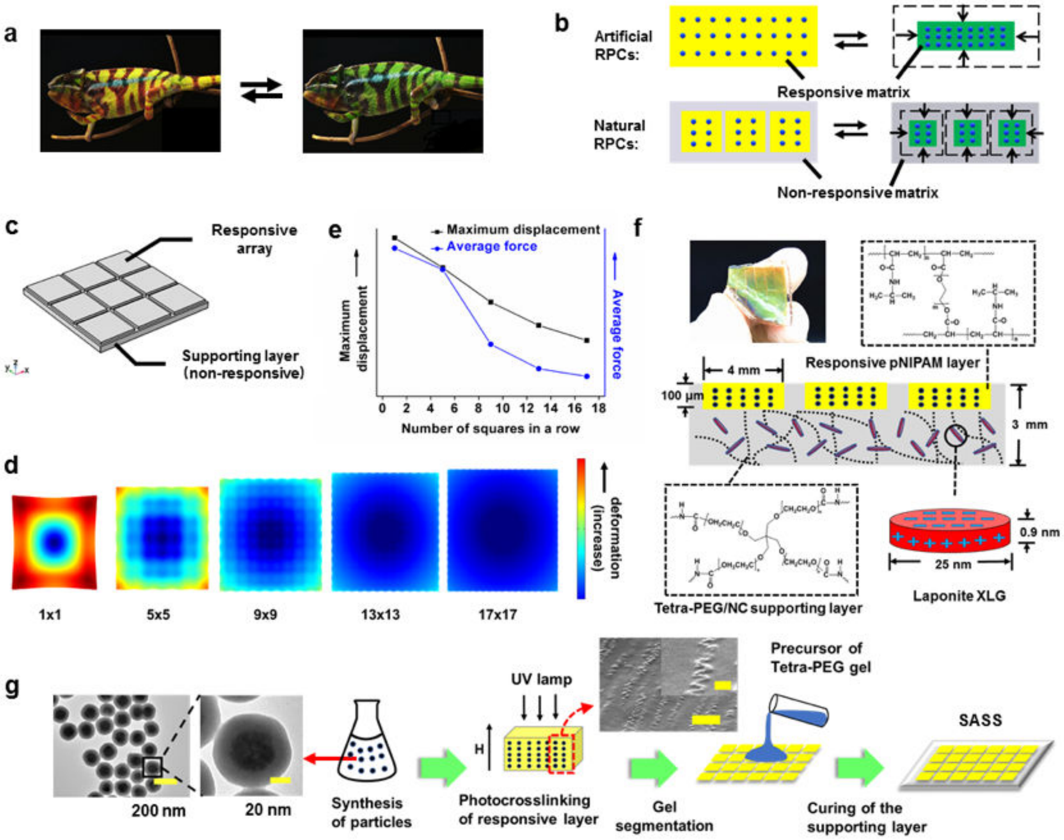

Figure 1.

Design and fabrication of strain-accommodating smart skin (SASS) material. (a) Photographs of a chameleon displaying color change[1] (Adapted with permission from Teyssier, J., Saenko, S. V., van der Marel, D. & Milinkovitch, M. C. *Nat. Commun.* 2015, *6*, 6368. Copyright 2015 Springer Nature). (b) Schematic comparing the typical design of artificial responsive PCs to responsive PCs utilized by nature. The dots represent the PC, yellow and green represent the swollen and de-swollen states of the responsive hydrogel, respectively, and gray indicates the supporting, non-responsive polymer matrix. (c) Model used for finite element analysis (FEA) of SASS (also see Supplementary S2). (d) Rendering of FEA model mapping the deformation of a bilayer material with a supporting non-responsive layer and a responsive upper layer divided into sections. (e) Plot of the FEA determined average force and maximal displacement within a plane of the supporting polymer layer as a function of the number of squares in the responsive PC array layer. (f) Photograph and schematic of SASS that includes dimensions and chemical structure of polymers. (g) Flow diagram illustrating the steps used in SASS fabrication, where TEM and SEM images show representative structures of the magnetic nanoparticles and their organization with responsive PC (Scale bar of SEM image: 5 µm and 1µm (inset)).

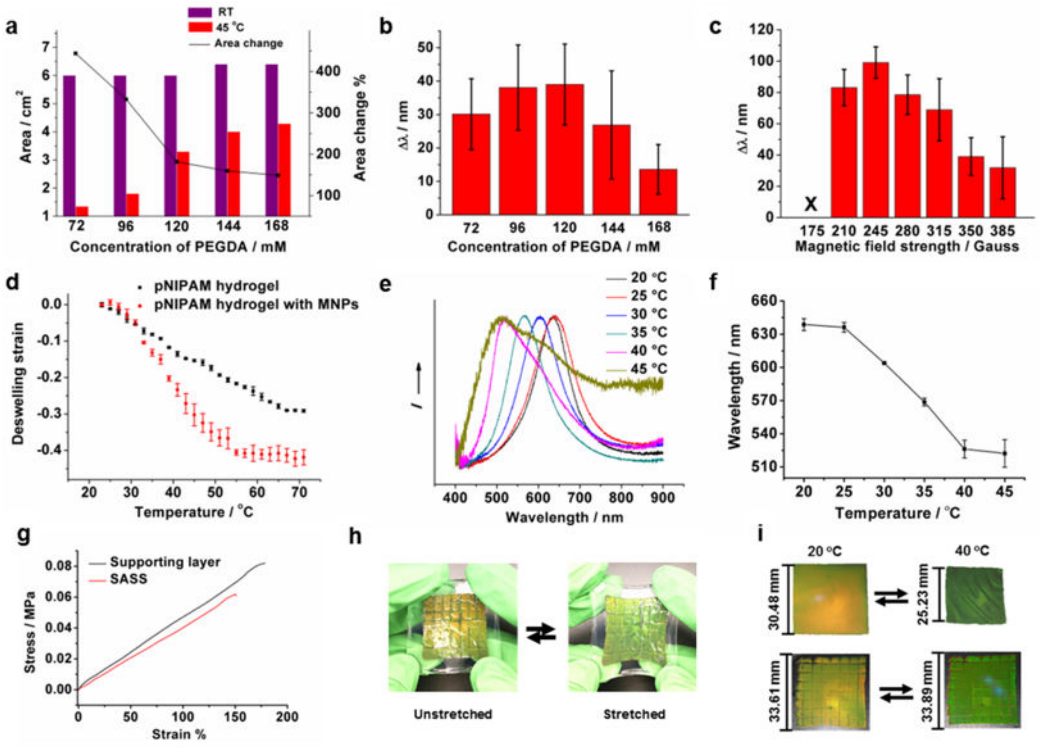

Figure 2.

Characterization of SASS. (a) Plot relating the crosslinker (PEGDA) concentration in pNIPAM PC gels to their area before and after heating to 45 °C (a 350 Gauss magnetic field was applied during polymerization). The right y-axis represents the area change % upon heating for each composition. (b) Plot showing the change in reflection λ_{max} for the samples prepared in (a). The $\Delta\lambda_{max}$ was determined using reflection spectra of standalone PC films at RT and 45 °C. (c) Plot of reflection $\Delta\lambda_{max}$ (collected at RT and 45 °C) for responsive pNIPAM PCs polymerized under different magnetic field strengths. These gels were synthesized with 120 mM PEGDA. (d) Plot of temperature-dependent strain of pNIPAM hydrogels prepared without (black) and with magnetic nanoparticles (red). (e) Normalized reflection spectra of a SASS sample collected at different temperatures. (f) Plot showing λ_{max} of reflectance for SASS samples as a function of temperature. (g) Representative uniaxial tensile measurement of a SASS sample (red) and a sample of a standalone film comprised of the strain-accommodating polymer (black). (h) Photographs demonstrating the elasticity of SASS and its strain-induced color change. (i) Photographs showing the chromatic response of a traditional responsive pNIPAM PC film (upper) triggered by adjusting the temperature (20 °C to 40 °C) compared to the chromatic response of SASS (lower) under the same conditions. The dimensions of the materials in the initial and final states are provided to the left of each image. All error bars represent the standard deviation of three independent measurements.

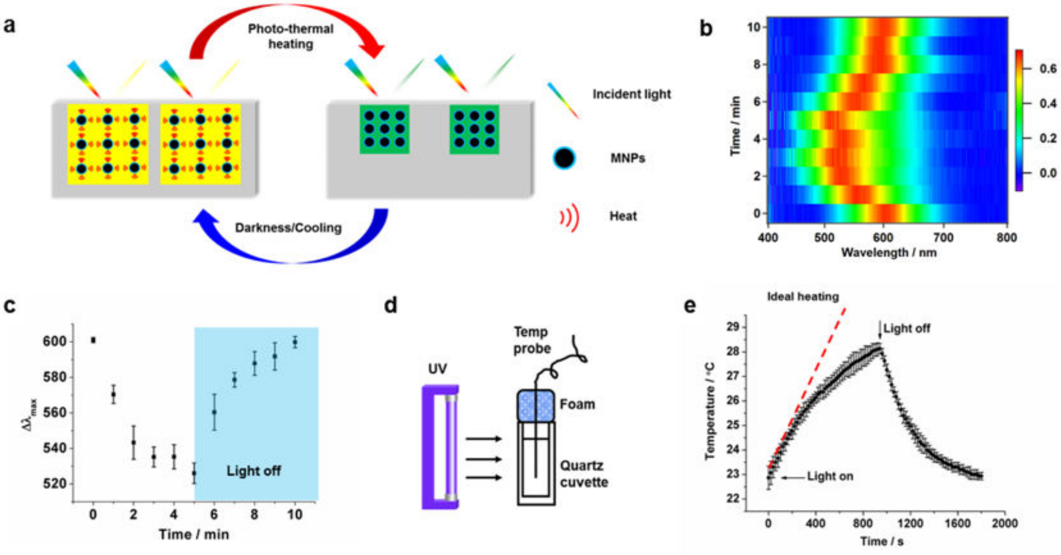

Figure 3.

Light responsive behavior of SASS. (a) Schematic of the light responsive mechanism of SASS. Exposure to white light induces photothermal heating and a concomitant spectral shift in the peak absorbance as the spacing within the PC decreases. Cessation of light returns SASS to its original state. (b) 2-Dimensional color map depicting the spectral shift of SASS as a function of time when exposed to a white light LED source (light was on 0-5 min and off 5-10 min). (c) The reflection λ_{max} of illuminated SASS samples as described in b. The error bars represent the standard deviation of three measurements obtained from three different SASS samples. (d) Schematic of equipment set-up used for measuring the photo-thermal conversion efficiency. A UV light source was used to illuminate a dispersion of MNPs while the solution temperature was measured. (e) Plot of solution temperature during exposure of MNP dispersion to UV light as a function of time. The error bar represents the standard deviation from three independent samples. The red dashed line indicates the ideal heating of the dispersion and provides the heating rate of the sample.

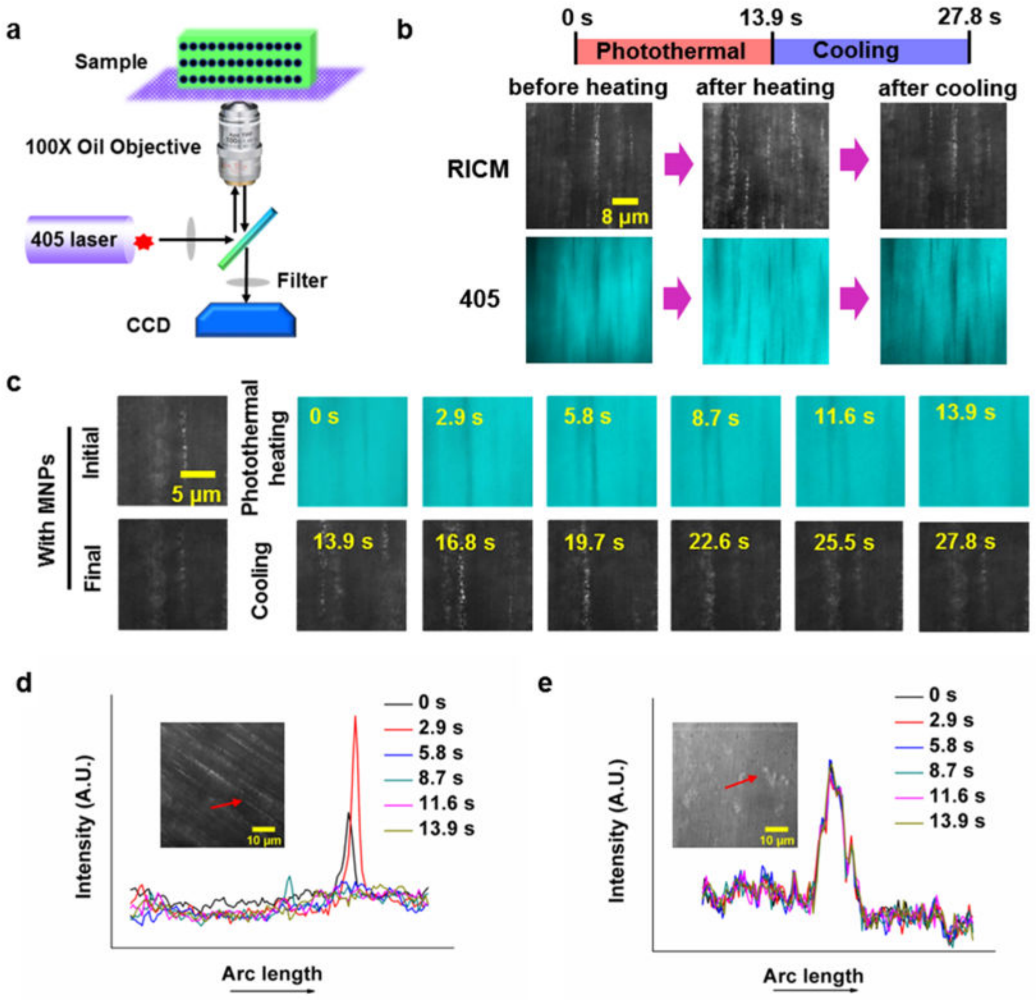

Figure 4.

Microscopic *in-situ* observation of the light-induced SASS response. (a) Schematic of the microscope and sample set-up for *in-situ* observation of SASS. Irradiation with a 405 nm laser initiates photothermal heating, and remodels MNP organization. (b) Images of aligned MNPs in the responsive layer captured upon initiation of photothermal heating (0 s), at the end of heating (13.9 s), and at the end of cooling (27.8 s). (c) Time-lapse images of aligned MNPs in the responsive layer collected during photothermal heating with a 405 nm laser and cooling with the laser off. (d) and (e) show plots of line-scans for $Fe_3O_4@SiO_2$ nanoparticles (~3 nM), and SiO_2 nanoparticles (~3 nM) embedded within pNIPAM hydrogels during relaxation following 405 nm excitation for 13.9 s.

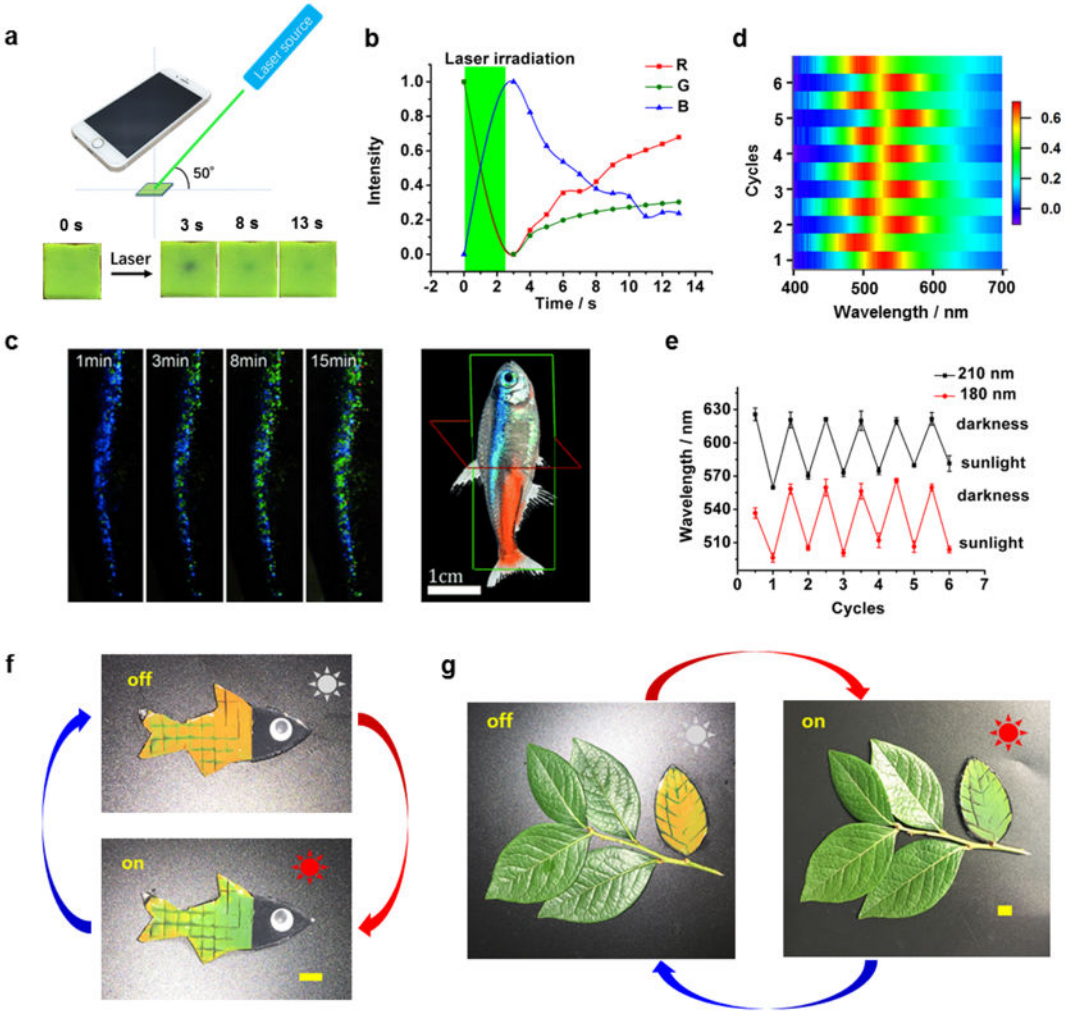

Figure 5.

Potential light-triggered applications of SASS materials. (a) Experimental diagram of SASS optical stimulation along with smart phone camera readout. Lower inset: Photograph of a single 4 mm × 4 mm SASS tile before and after exposure to 532 nm laser. The SASS sample was fabricated using 180 nm diameter particles. (b) Red, green, and blue (RGB) colorimetric analysis of SASS response following a laser pulse. The green area indicates the period of laser irradiation. (c) Time lapse images of the lateral strip of a neon tetra fish after exposure to sunlight (Adapted with permission from Gur, D. *et al.*, *Angew. Chem. Int. Ed.* 2015, *54,* 12426-12430. Copyright 2015 Wiley-VCH). (d) 2-Dimensional color map depicting the spectral shift during six sunlight triggered chromatic shift cycles. (e) Plot showing the chromatic shift of two SASS samples following multiple cycles of exposure to sunlight. The SASS samples were fabricated with two different sizes of MNPs. The maximum peak wavelength for each sample is plotted while oscillating between exposure to sunlight and darkness. (f) A fish-shaped SASS sample before (top) and after (bottom) exposure to sunlight for 10 min. (g) A camouflaged “leaf” fabricated with SASS and positioned alongside real leaves before (left) and after (right) sunlight exposure for 10 min (Scalebars: 1 cm).